



# Asynchronous current-induced switching of rare-earth and transition-metal sublattices in ferrimagnetic alloys

Giacomo Sala<sup>1</sup>✉, Charles-Henri Lambert<sup>1</sup>, Simone Finizio<sup>2</sup>, Victor Raposo<sup>3</sup>, Viola Krizakova<sup>1</sup>, Gunasheel Krishnaswamy<sup>1</sup>, Markus Weigand<sup>4</sup>, Jörg Raabe<sup>2</sup>, Marta D. Rossell<sup>5</sup>, Eduardo Martinez<sup>3</sup> and Pietro Gambardella<sup>1</sup>✉

**Ferrimagnetic alloys are model systems for understanding the ultrafast magnetization switching in materials with antiferromagnetically coupled sublattices. Here we investigate the dynamics of the rare-earth and transition-metal sublattices in ferrimagnetic GdFeCo and TbCo dots excited by spin-orbit torques with combined temporal, spatial and elemental resolution. We observe distinct switching regimes in which the magnetizations of the two sublattices either remain synchronized throughout the reversal process or switch following different trajectories in time and space. In the latter case, we observe a transient ferromagnetic state that lasts up to 2 ns. The asynchronous switching of the two magnetizations is ascribed to the master-agent dynamics induced by the spin-orbit torques on the transition-metal and rare-earth sublattices and their weak antiferromagnetic coupling, which depends sensitively on the alloy microstructure. Larger antiferromagnetic exchange leads to faster switching and shorter recovery of the magnetization after a current pulse. Our findings provide insight into the dynamics of ferrimagnets and the design of spintronic devices with fast and uniform switching.**

Ferrimagnetic alloys have raised strong interest owing to their ultrafast magneto-optical switching properties<sup>1–4</sup> and high speed current-induced magnetic domain-wall motion<sup>5–7</sup>. These characteristics make ferrimagnets optimal candidates for non-volatile memory applications<sup>4,8,9</sup>, as well as for testing models of magnetization dynamics in multi-element systems<sup>6,10–15</sup>. Several rare-earth (RE) transition-metal (TM) alloys are ferrimagnetic because the localized 4f magnetic moments of the RE and the itinerant 3d moments of the TM couple antiparallel to each other, forming two spin sublattices with distinct properties that can be tuned by composition and temperature<sup>16</sup>. In particular, the total magnetization and angular momentum vanish at the respective compensation points, which makes the magnetization dynamics immune to external fields and extremely fast.

These dynamics can be quite surprising. Intense laser pulses as short as 40 fs can toggle the magnetization of RE-TM ferrimagnets without the assistance of magnetic fields<sup>1,3,4</sup>. This all-optical switching involves an unusual transient ferromagnetic state<sup>17,18</sup> during which the RE and TM magnetizations attain the same orientation for a few picoseconds. The ferromagnetic alignment results from the interplay of ultrafast heating and the transfer of angular momentum between two spin sublattices with distinct demagnetization rates, and is instrumental in achieving fast switching<sup>13,14,19,20</sup>. Besides optical means, the magnetic order of RE-TM ferrimagnets can be manipulated by current-induced heat<sup>21,22</sup> and spin-orbit torques (SOT)<sup>23</sup>. Whereas intense picosecond-long heat pulses have a toggling effect similar to all-optical switching<sup>21,22</sup>, SOT induce bipolar switching<sup>24–27</sup> and directional domain-wall motion with velocities of up to 5 km s<sup>−1</sup>, close to the angular momentum compensation point<sup>5–7</sup>. In general, however,

the response of the RE and TM spin sublattices to an electric current can be more complex than considered so far, both in the temporal and spatial domains. In contrast to all-optical switching, for which the role of the RE and TM sublattices has been intensively investigated<sup>12,14,17,18</sup>, the RE and TM magnetic moments are considered to be steadily coupled to each other during current-induced switching and domain-wall motion, similar to antiferromagnets<sup>28,29</sup>. Testing this assumption is important to understand the SOT-induced dynamics of ferrimagnets as well as to optimize their magnetization reversal speed.

Here, we present a study of the SOT-induced magnetization switching of RE-TM ferrimagnets that combines time, space and element resolutions. By using scanning transmission X-ray microscopy (STXM) and X-ray magnetic circular dichroism (XMCD), we probe the evolution of the RE and TM magnetizations excited by subnanosecond- and nanosecond-long current pulses. While being antiferromagnetically coupled in equilibrium, the two sublattices can evolve asynchronously in time and inhomogeneously in space during and after the electric pulses. This difference takes the form of a delay between domain walls in the two sublattices or, in the extreme case, of a transient ferromagnetic state that can last as long as 2 ns. Our measurements, combined with micromagnetic simulations, reveal that the speed of the magnetization reversal in RE-TM ferrimagnets depends critically on the antiferromagnetic exchange coupling between the RE and TM sublattices, which is determined by the microstructure of the RE-TM alloy.

**Magnetization reversal of the TM and RE sublattices.** We employed a stroboscopic current-pump, X-ray-probe imaging technique to study amorphous ferrimagnetic alloys of GdFeCo

<sup>1</sup>Department of Materials, ETH Zurich, Zurich, Switzerland. <sup>2</sup>Swiss Light Source, Paul Scherrer Institut, Villigen, Switzerland. <sup>3</sup>Departamento de Física Aplicada, University of Salamanca, Salamanca, Spain. <sup>4</sup>Max Planck Institute for Intelligent Systems, Stuttgart, Germany. <sup>5</sup>Electron Microscopy Center, EMPA, Swiss Federal Laboratories for Materials Science and Technology, Dübendorf, Switzerland. ✉e-mail: [giacomo.sala@mat.ethz.ch](mailto:giacomo.sala@mat.ethz.ch); [pietro.gambardella@mat.ethz.ch](mailto:pietro.gambardella@mat.ethz.ch)

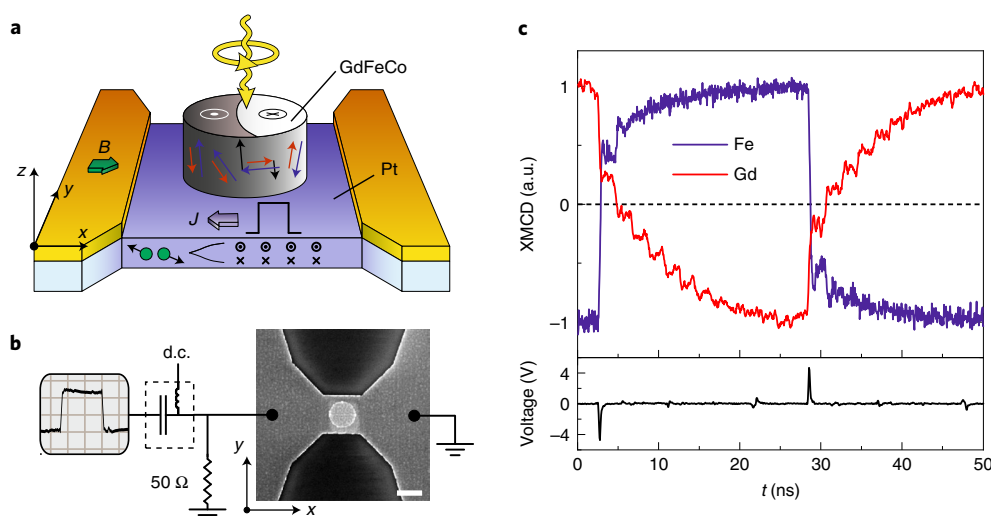


**Fig. 1 | Time-, space- and element-resolved current-induced switching of GdFeCo.** **a**, Schematic of the sample layout, which consists of a ferrimagnetic GdFeCo dot (black and white) on top of a Pt current line (blue). The electrical contacts are shown in yellow. The spin angular momentum induced by the current pulse  $J$  at the Pt surface (dotted circles and crosses) exerts spin-orbit torques of different magnitude (black arrows) on the TM and RE magnetic moments (red and blue arrows) and causes their switching by domain-wall motion. The yellow arrows represent the circularly-polarized X-rays. **b**, Scanning electron micrograph of the device and schematic of the electric set-up used for its excitation. The scale bar corresponds to 1 μm. **c**, Time dependence of the spatially averaged XMCD signal at the Fe  $L_3$  and Gd  $M_5$  edges measured while applying bipolar electric pulses with 200 ps duration (full-width at half-maximum) and 4.8 V amplitude ( $J \approx 1.3 \times 10^{12} \text{ A m}^{-2}$ ) to a Gd<sub>31</sub>Fe<sub>62</sub>Co<sub>7</sub> dot. A static magnetic field  $B = 25 \text{ mT}$  was applied parallel to the current direction to define the switching polarity. The bottom panel shows the amplitude and duration of the voltage pulses over time ( $t$ ). a.u., arbitrary units.

(15 nm) and TbCo (4 nm) with perpendicular anisotropy, shaped into circular dots with a diameter of 0.5 or 1 μm (Methods and Supplementary Notes 1 and 2). The dots were fabricated on top of a Pt layer (5 nm) that served for the injection of electric pulses, as shown in Fig. 1a,b. The devices were excited with a repeated sequence of set–reset pulses with alternating polarity that toggled the magnetization via the SOT<sup>23,30</sup>. The dynamics of the  $z$  magnetization component of each sublattice were detected by measuring the transmission through the sample of circularly polarized X-rays tuned to the  $L_3$  and  $M_5$  absorption edges of the TM and RE elements, respectively. The X-ray beam, which consisted of 70-ps-long X-ray pulses synchronized to the current excitation, was raster-scanned over the sample with a spatial resolution of 35 nm (Methods).

The XMCD traces in Fig. 1c represent the time dependence of the spatially averaged magnetic contrast measured at the Fe and Gd edges in a Gd<sub>31</sub>Fe<sub>62</sub>Co<sub>7</sub> dot excited by 200-ps-long electric pulses. The switching of a 1-μm-wide dot by 200 ps pulses confirms the fast current-induced dynamics of ferrimagnets. At equilibrium, Fe and Gd have opposite XMCD contrast, as expected from the anti-parallel orientation of their magnetizations,  $\mathbf{M}_{\text{Fe}}$  and  $\mathbf{M}_{\text{Gd}}$ . At each electric pulse, both  $\mathbf{M}_{\text{Fe}}$  and  $\mathbf{M}_{\text{Gd}}$  switch to the opposite state. Their final up or down orientation is determined by the polarity of the pulse and the direction of the magnetic field applied collinear to the current, as typical of SOT<sup>23,30</sup>. However, the reversal path followed by Fe and Gd is unexpected and very different from the switching trajectory observed in ferromagnets. First, rather than switching during the electric pulse<sup>31</sup>, the process involves two phases: an abrupt transition and a slow oscillatory evolution towards equilibrium that is particularly pronounced in Gd. Second, although both sublattices share this two-phase dynamic, they switch asynchronously with respect to each other, as indicated by the different times at which the traces cross zero. Whereas  $\mathbf{M}_{\text{Fe}}$  reverses its direction during the electric pulse,  $\mathbf{M}_{\text{Gd}}$  maintains its original orientation. Only 2 ns after the pulse onset does  $\mathbf{M}_{\text{Gd}}$  switch. Thus, the two magnetizations attain an average transient ferromagnetic state on the nanosecond timescale.

**Spatially resolved dynamics.** To better visualize the reversal process, we increased the pulse length to 1 ns, as shown in Fig. 2a. Similarly to the switching with 200 ps pulses, the reversal proceeds via a rapid transition and a slow oscillatory phase, with a temporary ferromagnetic alignment of the two sublattices that persists well beyond the end of the electrical excitation. The underlying switching process is clarified by the frames in Fig. 2b, which display snapshots of the magnetization in the two sublattices. The reversal of  $\mathbf{M}_{\text{Fe}}$  involves the nucleation of a domain at the edge of the dot and the motion of a domain wall across the device with a speed of 0.8–1.3 km s<sup>−1</sup>, depending on the applied current density. We attribute this behaviour to the interplay of SOT, the Dzyaloshinskii–Moriya interaction and the magnetic field, in analogy to ferromagnetic systems<sup>31,32</sup>.

The dynamics of the Gd sublattice are substantially slower than those of Fe. No clear domain wall appears in Gd during the pulse. Instead, the magnetic contrast diminishes starting from the edges, but only partially, so that  $\mathbf{M}_{\text{Fe}}$  and  $\mathbf{M}_{\text{Gd}}$  attain the same orientation at the end of the pulse, as exemplified in the sketch in Fig. 2b. Only 1 ns after the pulse, a domain appears to expand in the Gd sublattice from the left to the right side, thus reestablishing the antiferromagnetic alignment between Gd and Fe. After about 3 ns from the onset of the pulse, no additional changes are observed in the two sublattices apart from a progressive increase of the magnetic contrast (Supplementary Video 1). This intensification corresponds to the slow after-pulse dynamics evidenced by Figs. 1c and 2a, which are also accompanied by temporal oscillations of the magnetic contrast. Micromagnetic simulations identify the origin of the slow dynamics and its oscillations with the combination of delayed domain nucleation events and collective magnetization precession, as discussed later. Our measurements show that this behaviour is observed for both down–up and up–down switching upon reversing the polarity of the current; is independent of the pulse length or amplitude and the strength of the in-plane magnetic field; and is not caused by Joule heating. Finally, we do not identify differences between the magnetization of Fe and Co, which remain ferromagnetically coupled (Supplementary Notes 3–5).

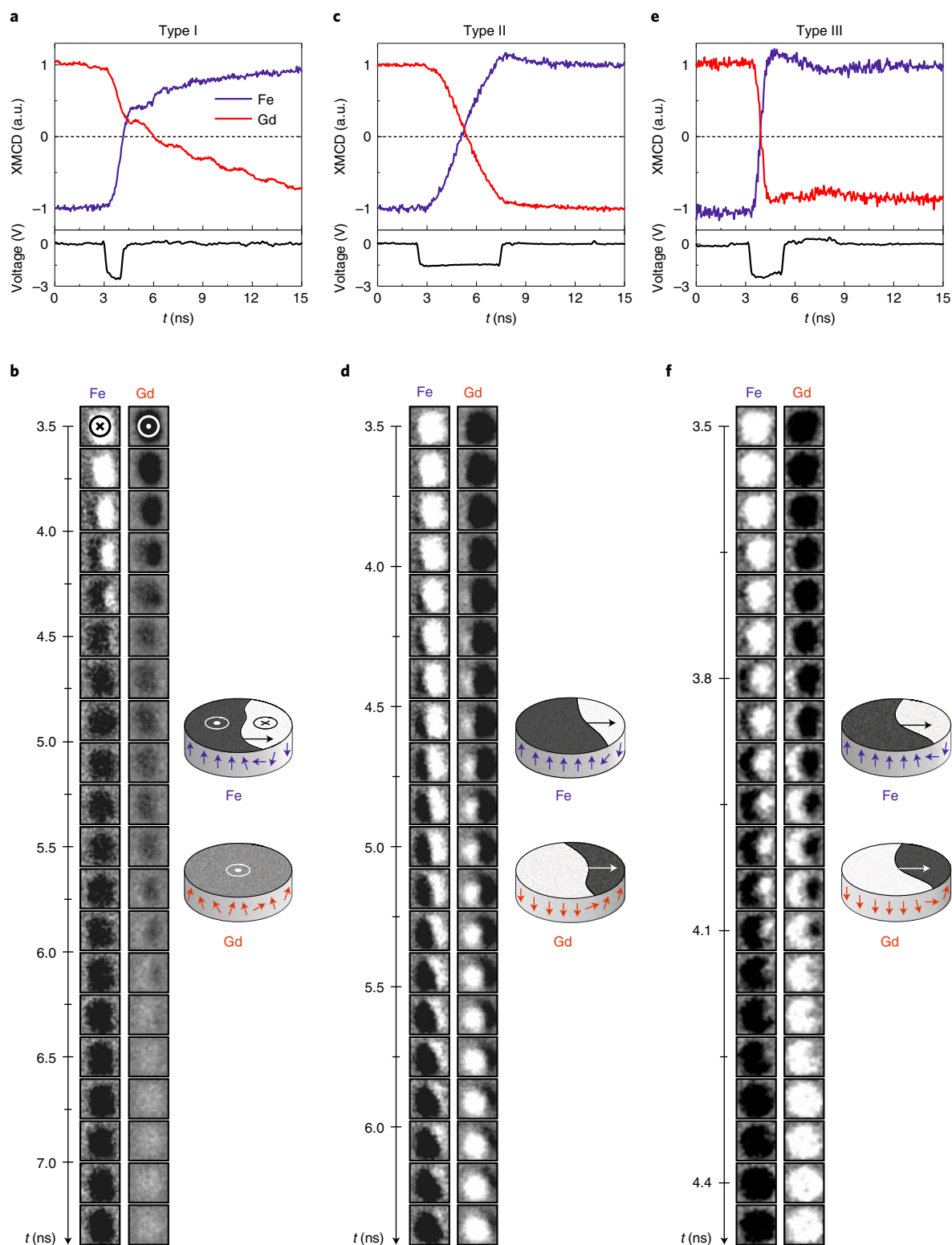


**Fig. 2 | Switching dynamics of GdFeCo. a,c,e**, Time dependence of the spatially averaged XMCD contrast at the Fe and Gd edges for three distinct devices. The device composition is  $\text{Gd}_{31}\text{Fe}_{62}\text{Co}_7$ ,  $\text{Gd}_{30}\text{Fe}_{63}\text{Co}_7$  and  $\text{Gd}_{29}\text{Fe}_{64}\text{Co}_7$  in **a**, **c** and **e**, respectively. The electric pulses, plotted in the bottom panels, have a duration of 1 ns, 5 ns or 2 ns and amplitude of -2.5 V, -1.4 V or -2.3 V, respectively. A voltage of 2.5 V corresponds to a current density of  $-0.7 \times 10^{12} \text{ A m}^{-2}$ . The in-plane magnetic field was 20 mT, 10 mT and 20 mT, respectively. **b,d,f**, Snapshots of the dynamics in **a**, **c** and **e**, respectively. The schematics show the orientation of the magnetic moments of Fe (blue arrows) and Gd (red arrows) during the switching, the profile of the domain wall and the domain wall's direction of motion (black arrow). The vertical axis defines the timing (in nanoseconds) of the frames, which have a dimension of  $1.2 \times 1.2 \mu\text{m}^2$ . The dynamics in **a** and **b** were measured in the same device as in Fig. 1c.

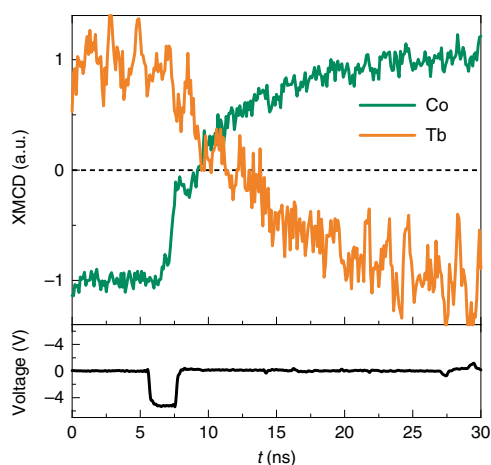


**Fig. 3 | Switching dynamics of TbCo.** Time dependence of the spatially averaged XMCD contrast at the Co and Tb edges of a 500-nm-wide  $\text{Tb}_{19}\text{Co}_{81}$  dot excited by 2-ns-long electric pulses with 5.1 V amplitude. The in-plane magnetic field was 110 mT.

Beside these dynamics, which we label type I, we found two additional switching regimes in devices that differ in their microstructure and composition. These regimes, unlike the type I regime, involve a single phase that terminates before the end of the pulse without further slow changes of the magnetization. In addition, domain walls move in both sublattices. The type II dynamics, shown in Fig. 2c,d, are characterized by the asynchronous motion of the Fe and Gd domain walls, which are decoupled, both in time, with a small but measurable delay of about 200 ps, and in space, with different profiles across the dot (Supplementary Note 3 and Supplementary Video 2).

Last,  $\mathbf{M}_{\text{Fe}}$  and  $\mathbf{M}_{\text{Gd}}$  can also switch by preserving antiparallel coupling throughout the whole process. In these type III dynamics, the edge nucleation of a domain occurs at the same time in Fe and Gd, and the domain walls propagate together without a measurable delay (Supplementary Video 3). The type III regime corresponds to the scenario normally assumed in the modelling of current-induced switching and domain-wall motion in ferrimagnets, namely, the rigid antiferromagnetic coupling between the two sublattices.

These unexpected dynamics are not limited to GdFeCo.  $\text{Tb}_{1-x}\text{Co}_x$  (4) alloys and  $(\text{Tb}(0.25)/\text{Co}(0.25))_{\text{x}}$  multilayers also present asynchronous switching regimes (Supplementary Note 6). For example, Fig. 3 shows the temporal evolution of the spatially averaged XMCD contrast measured at the Tb and Co edges in a  $\text{Tb}_{19}\text{Co}_{81}$  dot excited by 2-ns-long current pulses. The small thickness of TbCo limits the signal quality and hinders the detection of the spatial details of the dynamics. However, the traces present the same features as the type I dynamics of GdFeCo, namely, the faster switching of the TM sublattice and a ferromagnetic state lasting for about 1 ns.

These measurements disclose the existence of multiple switching paths in RE-TM ferrimagnets characterized by a variable degree of coupling between the two sublattices. Extensive experiments confirm that this variability is an intrinsic property of each sample, independent of the amplitude and duration of the electric pulses, as well as of the applied magnetic field (Supplementary Note 4). Moreover, the type of dynamics is not simply associated with the sample stoichiometry because devices with equal composition show distinct reversal regimes (Supplementary Note 6).

**Micromagnetic modelling.** To rationalize such diversified dynamics, we performed micromagnetic simulations of the switching caused by SOT in RE-TM ferrimagnets, in which  $\mathbf{M}_{\text{Fe}}$  and  $\mathbf{M}_{\text{Gd}}$  are

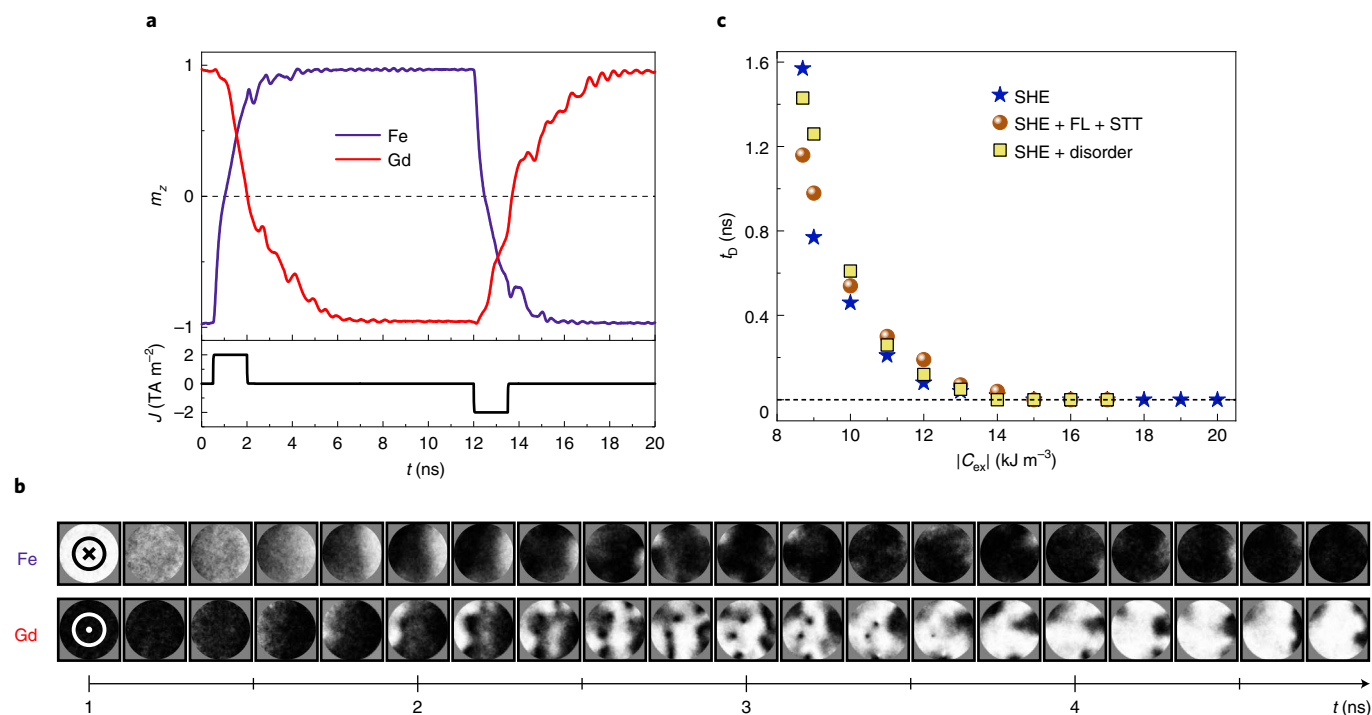
separately described by two coupled Landau-Lifschitz-Gilbert equations (Methods and the literature<sup>33</sup>). Since the major contribution to  $\mathbf{M}_{\text{Gd}}$  comes from the localized 4f electrons, which lie about 4 eV below the Fermi level, the magneto-transport properties of RE-TM ferrimagnets depend mostly on the 3d electrons of the TM element<sup>34–37</sup>. Thus, the SOT are expected to interact predominantly with the TM magnetic moments and be transferred to the RE sublattice indirectly through the RE-TM exchange interaction. This imbalance was taken into account by adopting element-dependent effective spin Hall angles. In this scenario, our simulations reproduce the three types of dynamics under the assumption of a variable antiferromagnetic coupling, whose strength is modelled by the exchange energy per unit volume  $C_{\text{ex}}$  (Methods and Supplementary Note 7). In the following, we consider GdFeCo as model system, but similar considerations apply to TbCo.

Figure 4a,b shows the simulated dynamics of the Fe and Gd sublattices triggered by 1.5-ns-long pulses with  $2 \times 10^{12} \text{ A m}^{-2}$  current density, assuming effective spin Hall angles of  $\theta_{\text{SH}}^{\text{TM}} = 0.21$  and  $\theta_{\text{SH}}^{\text{RE}} = 0.07$  and  $C_{\text{ex}} = -6.8 \text{ kJ m}^{-3}$ . The simulations reproduce all the main features of the type I dynamics shown in Figs. 1c and 2a,b, namely, the switching by domain nucleation and propagation in Fe but not in Gd; the formation of the transient ferromagnetic state; and the after-pulse slow recovery of the magnetization. Upon injection of the pulse, the SOT trigger the switching of  $\mathbf{M}_{\text{Fe}}$ . For a sufficiently large current, this process is almost instantaneous<sup>27</sup>. However, since the effect of the SOT on  $\mathbf{M}_{\text{Gd}}$  is small, the latter can switch only if dragged by the antiferromagnetic exchange torque<sup>38</sup>. This is a turbulent process without a reproducible spatial pattern because it develops when  $\mathbf{M}_{\text{Fe}}$  has already completed the switching, which results in the weak homogeneous XMCD contrast, as observed in Fig. 2b. At the same time, the average perpendicular component of  $\mathbf{M}_{\text{Gd}}$  oscillates around the total perpendicular field resulting from the exchange and anisotropy fields, in agreement with the oscillations visible in Figs. 1c and 2a.

The switching dynamics transition from type I to type III in a narrow range of  $C_{\text{ex}}$  (Fig. 4c and Supplementary Notes 9 and 10). For  $|C_{\text{ex}}| \geq 11 \text{ kJ m}^{-3}$ , the switching is mediated by the displacement of a domain wall in both the Fe and Gd sublattices. A finite delay exists between the two domain walls for intermediate values of  $C_{\text{ex}}$ , whereas for  $|C_{\text{ex}}| \geq 14 \text{ kJ m}^{-3}$  the two magnetizations remain rigidly coupled during the entire process. Small variations of the saturation magnetization and magnetic anisotropy lead to better agreement of the simulations of different samples, but are not essential to reproduce the type of dynamics. Simulations performed for different values of the applied magnetic field, spin-transfer torque (STT), field-like SOT and Dzyaloshinskii-Moriya interaction or by including thermal fluctuations, defects and random spatial variations of the magnetic parameters do not reproduce the transition between the three dynamics regimes. The precise value of  $\theta_{\text{SH}}^{\text{RE}}$  is also not fundamental to reproduce the experimental dynamics provided that  $\theta_{\text{SH}}^{\text{RE}} < \theta_{\text{SH}}^{\text{TM}}$ . Thus, the sole parameter that allows us to replicate the nanosecond-long ferromagnetic state and the change of switching regime is  $C_{\text{ex}}$ .

We summarize these findings in Fig. 4c by simulating the delay time  $t_{\text{D}}$  of  $\mathbf{M}_{\text{Gd}}$  with respect to  $\mathbf{M}_{\text{Fe}}$  as a function of  $C_{\text{ex}}$  (all of the other parameters are fixed). We find that  $t_{\text{D}}$  rapidly diminishes as  $C_{\text{ex}}$  becomes larger, and the increase also results in an overall faster dynamics, as expected for antiferromagnets (Supplementary Note 11). The simulations clarify that the asynchronous switching originates from the weak and variable antiferromagnetic coupling between the RE and TM sublattices in conjunction with the master-agent dynamics induced by the SOT. While the latter is ascribed to the different localization of the electronic orbitals and density of states at the Fermi level of the RE and TM elements<sup>35–37</sup>, we find that the former is linked to the composition and microstructure of the ferrimagnetic alloy, as discussed next.





**Fig. 4 | Micromagnetic simulations of the asynchronous dynamics.** **a**, Time dependence of the simulated average component  $m_z$  of  $\mathbf{M}_{\text{Fe}}$  and  $\mathbf{M}_{\text{Gd}}$  excited by an electric pulse with 1.5 ns duration and a current density of 2 TA m<sup>-2</sup> when  $C_{\text{ex}} = -6.8$  kJ m<sup>-3</sup>. **b**, Snapshots of the magnetization switching induced by the first electric pulse in **a**. **c**, Delay  $t_0 = t_{\text{Fe}} - t_{\text{Gd}}$  between the times at which the  $m_z$  components of  $\mathbf{M}_{\text{Fe}}$  and  $\mathbf{M}_{\text{Gd}}$  cross zero as a function of the antiferromagnetic exchange energy density  $|C_{\text{ex}}|$ . The simulations assume the damping-like spin Hall effect (SHE) with spin Hall angles  $\theta_{\text{SH}}^{\text{TM}} = 0.21$  and  $\theta_{\text{SH}}^{\text{RE}} = 0.07$  (stars); the damping-like SHE including the field-like (FL) torque and STT (circles); and the damping-like SHE and thermal fluctuations and grains of 10 nm size with 10% random variations of the magnetic anisotropy (squares; Methods and Supplementary Note 8).

**Discussion and outlook.** The asynchronous sublattice magnetization dynamics reported here are reminiscent of the all-optical switching observed in GdFeCo alloys<sup>3,4,17,18</sup>. Yet our measurements show that the decoupling of the RE and TM magnetization dynamics is a general feature of RE-TM alloys that extends well beyond the ultrafast temporal regime of all-optical switching and also involves spin torque excitations. Moreover, in contrast with the toggling of the magnetization induced by ultrafast heat pulses<sup>21</sup>, the switching of GdFeCo and TbCo induced by SOT depends on the polarity of the current and is not limited to picosecond-long pulses. Joule heating associated with the current plays a role in activating domain nucleation<sup>27</sup>, but the temperature increase in our devices is too slow and moderate ( $<8$  K ns<sup>-1</sup>; Supplementary Note 5) to induce thermal toggling of the magnetization<sup>21</sup>. Another specific feature of current-induced switching is the coherent domain-wall motion in the TM sublattice accompanied by either disordered or delayed domain-wall dynamics in the Gd sublattice in the type I or type II switching, respectively. Most importantly, a transient ferromagnetic state is not a prerequisite for switching, as indeed observed in the type III dynamics, because the reversal can directly occur due to the net transfer of angular momentum from the electric current to the magnetization. Besides these phenomenological considerations, all-optical and current-induced switching are fundamentally different because ultrafast heating involves relaxation of the longitudinal magnetization, whereas the spin torque dynamics are determined by the relaxation of the transverse component of the magnetization. The relaxation rate is proportional to the RE-TM exchange coupling in the first case, and to the effective magnetic field generated by the SOT in the second case<sup>39</sup>. Therefore, the observation of a nanosecond-long non-equilibrium ferromagnetic state cannot be explained by the thermal collapse of the longitudinal magnetization

of the TM sublattice, as in all-optical switching. Such a long-lived transient state can be rationalized only by assuming uneven transfer of angular momentum from the electric current to the TM and RE sublattices and a relatively weak coupling among them, in agreement with the results of our micromagnetic simulations. The combination of these two factors is responsible for the master-agent dynamics between the TM and RE magnetization observed in type I and II switching.

Measurements performed in a period of one year in 20 devices differing in composition and age indicate a correlation between the time passed since the sample growth and the change of the dynamics from type I to type III as the samples aged (Supplementary Note 6). Although changes of stoichiometry can also play a role, this trend suggests that ageing processes most affect the antiferromagnetic coupling between the RE and TM sublattices. To test this possibility, we have characterized nominally identical ‘fresh’ and ‘aged’ GdFeCo samples using scanning transmission electron microscopy (STEM) and energy-dispersive X-ray spectroscopy (EDX; Methods). The structural and elemental maps in Fig. 5 show that GdFeCo has an amorphous structure with nanoscale inhomogeneous distributions of Fe, Co and Gd. This inhomogeneity is present in both samples, but is more pronounced in the fresh sample, where the degree of anticorrelation between Fe and Gd is highest as estimated from the elemental concentration profiles (Fig. 5c,f) and autocorrelation maps (Fig. 5g and Supplementary Note 13). The existence of atomic clusters is further confirmed by nanobeam electron diffraction measurements, which reveal the presence of nanometre-size crystallites of Gd and Fe atoms that tend to intermix upon ageing. These results show that phase segregation takes place in RE-TM films, in agreement with previous studies<sup>20,40–44</sup>. An atomistic model of the antiferromagnetic energy density  $C_{\text{ex}}$

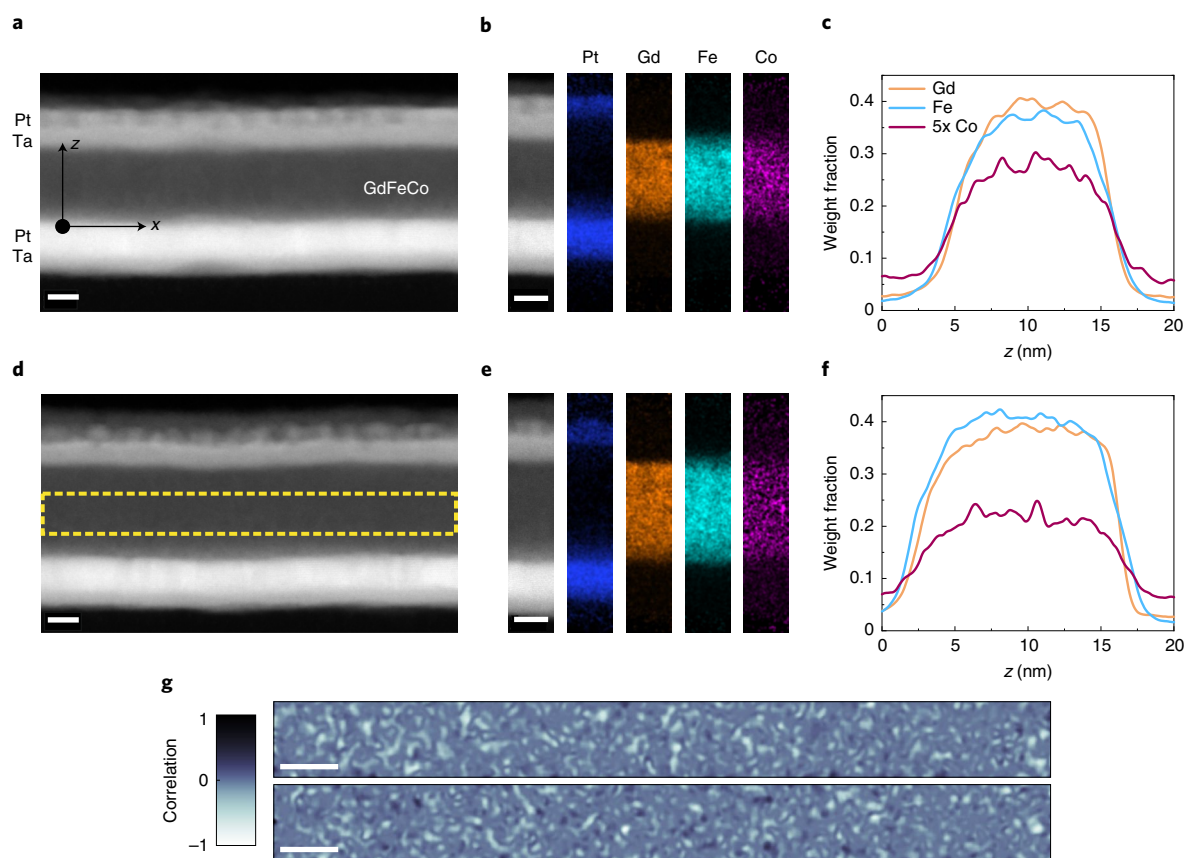


**Fig. 5 | Microstructure of fresh and aged GdFeCo films.** **a**, STEM micrograph of a  $\text{Gd}_{31}\text{Fe}_{62}\text{Co}_7$  blanket film characterized one month after growth. **b**, Magnified STEM image and STEM-EDX elemental maps of the constitutive elements. **c**, Profiles of the Gd, Fe and Co concentrations across the sample thickness. The concentration of Co has been multiplied by five to ease the comparison. The profiles are averaged along the x direction in **a**. **d–f**, The same as **a–c** for a nominally identical sample deposited simultaneously to the device in Figs. 1c and 2a,b and characterized 30 months after growth. **g**, Correlation image of the Fe and Gd concentration in the fresh (top) and aged (bottom) samples corresponding to the dashed rectangle in **d**. The correlation coefficients calculated from the two images are  $-0.50$  and  $-0.40$ , respectively. The correlation coefficients obtained from the Fe and Gd line profiles are  $-0.65$  and  $-0.37$  in the fresh and aged samples, respectively; Methods and Supplementary Note 13. The scale bars correspond to 5 nm.

demonstrates the sensitivity of this parameter to the microstructure of ferrimagnets (Supplementary Note 7). Although our simplified calculation does not take into account the full structural and magnetic complexity of these materials (Supplementary Notes 7 and 13), it shows that the formation of Gd-rich and Fe-rich clusters reduces the intersublattice coupling relative to the homogeneous phase by limiting the number of direct Fe–Gd interactions<sup>45</sup>. This reduction may be further enhanced by the sperimagnetic order typical of RE–TM ferrimagnets<sup>46,47</sup>, which leads to a distribution of interatomic exchange interactions. However, since the mixing enthalpy of TM and RE atoms is negative<sup>48</sup>, the intermixing of the two species increases with time<sup>49,50</sup>, in agreement with our STEM and electron diffraction observations. This structural relaxation affects  $C_{\text{ex}}$  and, ultimately, the type of dynamics during the SOT-induced switching.

In conclusion, our measurements reveal that the RE and TM sublattices of ferrimagnetic alloys can respond either synchronously or asynchronously to spin torques. We observe domain-wall speeds exceeding  $1 \text{ km s}^{-1}$  and switching with 200-ps-long current pulses in  $1\text{-}\mu\text{m}$ -wide devices. These rapid dynamics are the fingerprint of ferrimagnets. However, the two magnetic sublattices are not rigidly coupled and respond differently to SOT, which leads to spatially and temporally inhomogeneous dynamics. We identified three switching regimes, characterized by domain nucleation and propagation in the TM sublattice and (1) a transient ferromagnetic state followed

by slow and spatially inhomogeneous reversal of the RE sublattice (type I), (2) delayed domain-wall propagation in the RE sublattice (type II) and (3) synchronous switching of the RE sublattice (type III). Micromagnetic simulations rationalize this behaviour in terms of the antiferromagnetic exchange energy density, which varies in response to thermodynamically driven relaxation processes that alter the atomic structure of the RE–TM alloy. Our results have practical implications for tuning the composition and microstructure of ferrimagnetic alloys utilized in spintronic devices to achieve maximum and uniform switching speed with minimal after-pulse dynamics. Moreover, they provide insight into the magnetization reversal of antiferromagnetically coupled systems that complements that obtained for all-optical switching at ultrafast timescales.

### Online content

Any methods, additional references, Nature Research reporting summaries, source data, extended data, supplementary information, acknowledgements, peer review information; details of author contributions and competing interests; and statements of data and code availability are available at <https://doi.org/10.1038/s41563-022-01248-8>.

Received: 11 May 2021; Accepted: 4 April 2022;  
Published online: 12 May 2022

## References

- Stanciu, C. D. et al. All-optical magnetic recording with circularly polarized light. *Phys. Rev. Lett.* **99**, 047601 (2007).
- Vahaplar, K. et al. Ultrafast path for optical magnetization reversal via a strongly nonequilibrium state. *Phys. Rev. Lett.* **103**, 66–69 (2009).
- Kirilyuk, A., Kimel, A. V. & Rasing, T. Laser-induced magnetization dynamics and reversal in ferrimagnetic alloys. *Rep. Prog. Phys.* **76**, 026501 (2013).
- Kimel, A. V. & Li, M. Writing magnetic memory with ultrashort light pulses. *Nat. Rev. Mater.* **4**, 189–200 (2019).
- Siddiqui, S. A., Han, J., Finley, J. T., Ross, C. A. & Liu, L. Current-induced domain wall motion in a compensated ferrimagnet. *Phys. Rev. Lett.* **121**, 057701 (2018).
- Caretta, L. et al. Fast current-driven domain walls and small skyrmions in a compensated ferrimagnet. *Nat. Nanotechnol.* **13**, 1154–1160 (2018).
- Cai, K. et al. Ultrafast and energy-efficient spin-orbit torque switching in compensated ferrimagnets. *Nat. Electron.* **3**, 37–42 (2020).
- Yang, S. H., Ryu, K. S. & Parkin, S. Domain-wall velocities of up to 750 m s<sup>-1</sup> driven by exchange-coupling torque in synthetic antiferromagnets. *Nat. Nanotechnol.* **10**, 221–226 (2015).
- Lalieu, M. L., Lavrijsen, R. & Koopmans, B. Integrating all-optical switching with spintronics. *Nat. Commun.* **10**, 1–6 (2019).
- Ostler, T. A. et al. Crystallographically amorphous ferrimagnetic alloys: Comparing a localized atomistic spin model with experiments. *Physical Review B* **84**, 110 (2011).
- Schellekens, A. J. & Koopmans, B. Microscopic model for ultrafast magnetization dynamics of multisublattice magnets. *Phys. Rev. B* **87**, 020407 (2013).
- Atxitia, U., Barker, J., Chantrell, R. W. & Chubykalo-Fesenko, O. Controlling the polarity of the transient ferromagneticlike state in ferrimagnets. *Phys. Rev. B* **89**, 224421 (2014).
- Davies, C. et al. Pathways for single-shot all-optical switching of magnetization in ferrimagnets. *Phys. Rev. Appl.* **13**, 024064 (2020).
- Jakobs, F. et al. Unifying femtosecond and picosecond single-pulse magnetic switching in Gd-Fe-Co. *Phys. Rev. B* **103**, 104422 (2021).
- Haltz, E., Krishnia, S., Berges, L., Mouglin, A. & Sampaio, J. Domain wall dynamics in antiferromagnetically coupled double-lattice systems. *Phys. Rev. B* **103**, 014444 (2021).
- Buschow, K. H. J. Intermetallic compounds of rare-earth and 3d transition metals. *Rep. Prog. Phys.* **40**, 1179–1256 (1977).
- Radu, I. et al. Transient ferromagnetic-like state mediating ultrafast reversal of antiferromagnetically coupled spins. *Nature* **472**, 205–208 (2011).
- Ostler, T. A. et al. Ultrafast heating as a sufficient stimulus for magnetization reversal in a ferrimagnet. *Nat. Commun.* **3**, 666 (2012).
- Mentink, J. H. et al. Ultrafast spin dynamics in multisublattice magnets. *Phys. Rev. Lett.* **108**, 057202 (2012).
- Graves, C. E. et al. Nanoscale spin reversal by non-local angular momentum transfer following ultrafast laser excitation in ferrimagnetic GdFeCo. *Nat. Mater.* **12**, 293–298 (2013).
- Yang, Y. et al. Ultrafast magnetization reversal by picosecond electrical pulses. *Sci. Adv.* <https://doi.org/10.1126/sciadv.1603117> (2017).
- Wilson, R. B. et al. Ultrafast magnetic switching of GdFeCo with electronic heat currents. *Phys. Rev. B* **95**, 180409(R) (2017).
- Manchon, A. et al. Current-induced spin-orbit torques in ferromagnetic and antiferromagnetic systems. *Rev. Mod. Phys.* **91**, 035004 (2019).
- Mishra, R. et al. Anomalous current-induced spin torques in ferrimagnets near compensation. *Phys. Rev. Lett.* **118**, 167201 (2017).
- Roschewsky, N., Lambert, C.-H. & Salahuddin, S. Spin-orbit torque switching of ultrathin ferrimagnetic GdFeCo. *Phys. Rev. B* **96**, 064406 (2017).
- Je, S.-G. et al. Spin-orbit torque-induced switching in ferrimagnetic alloys: experiments and modeling. *Appl. Phys. Lett.* **112**, 062401 (2018).
- Sala, G. et al. Real-time Hall-effect detection of current-induced magnetization dynamics in ferrimagnets. *Nat. Commun.* **12**, 656 (2021).
- Gomonay, O., Jungwirth, T. & Sinova, J. High antiferromagnetic domain wall velocity induced by Néel spin-orbit torques. *Phys. Rev. Lett.* **117**, 017202 (2016).
- Shiino, T. et al. Antiferromagnetic domain wall motion driven by spin-orbit torques. *Phys. Rev. Lett.* **117**, 087203 (2016).
- Miron, I. M. et al. Perpendicular switching of a single ferromagnetic layer induced by in-plane current injection. *Nature* **476**, 189–193 (2011).
- Baumgartner, M. et al. Spatially and time-resolved magnetization dynamics driven by spin-orbit torques. *Nat. Nanotechnol.* **12**, 980–986 (2017).
- Martinez, E. et al. Universal chiral-triggered magnetization switching in confined nanodots. *Sci. Rep.* **5**, 10156 (2015).
- Martinez, E., Raposo, V. & Alejos, Ó. Current-driven domain wall dynamics in ferrimagnets: micromagnetic approach and collective coordinates model. *J. Magn. Magn. Mater.* **491**, 165545 (2019).
- Bellouard, C. et al. Negative spin-valve effect in Co<sub>65</sub>Fe<sub>35</sub>/Ag/(Co<sub>65</sub>Fe<sub>35</sub>)<sub>50</sub>Gd<sub>50</sub> trilayers. *Phys. Rev. B* **53**, 5082–5085 (1996).
- Tanaka, H., Takayama, S. & Fujiwara, T. Electronic-structure calculations for amorphous and crystalline Gd<sub>3</sub>Fe<sub>67</sub> alloys. *Phys. Rev. B* **46**, 7390–7394 (1992).
- Zhou, W., Seki, T., Kubota, T., Bauer, G. E. & Takanashi, K. Spin-Hall and anisotropic magnetoresistance in ferrimagnetic Co-Gd/Pt layers. *Phys. Rev. Mater.* **2**, 094404 (2018).
- Lim, Y. et al. Dephasing of transverse spin current in ferrimagnetic alloys. *Phys. Rev. B* **103**, 24443 (2021).
- Blasing, R. et al. Exchange coupling torque in ferrimagnetic Co/Gd bilayer maximized near angular momentum compensation temperature. *Nat. Commun.* **9**, 4984 (2018).
- Chubykalo-Fesenko, O., Nowak, U., Chantrell, R. W. & Garanin, D. Dynamic approach for micromagnetics close to the Curie temperature. *Phys. Rev. B* **74**, 094436 (2006).
- Liu, T.-M. et al. Nanoscale confinement of all-optical magnetic switching in TbFeCo - competition with nanoscale heterogeneity. *Nano Lett.* **15**, 6862–6868 (2015).
- Kirk, E. et al. Anisotropy-induced spin reorientation in chemically modulated amorphous ferrimagnetic films. *Phys. Rev. Mater.* **4**, 074403 (2020).
- Li, Z. G., Smith, D. J. & Marinero, E. E. Investigations of microstructure of thin TbFeCo films by high-resolution electron microscopy. *J. Appl. Phys.* **69**, 6590 (1991).
- Krishnia, S. et al. Spin-orbit coupling in single-layer ferrimagnets: direct observation of spin-orbit torques and chiral spin textures. *Phys. Rev. Appl.* **16**, 024040 (2021).
- Mimura, Y., Imamura, N., Kobayashi, T., Okada, A. & Kushiroya, Y. Magnetic properties of amorphous alloy films of Fe with Gd, Tb, Dy, Ho, or Er. *J. Appl. Phys.* **49**, 1208–1215 (1978).
- Beens, M., Lalieu, M. L., Duine, R. A. & Koopmans, B. The role of intermixing in all-optical switching of synthetic-ferrimagnetic multilayers. *AIP Adv.* **9**, 125133 (2019).
- Taylor, R. C. & Gangulee, A. Magnetic properties of 3d transition metals in the amorphous ternary alloys: Gd<sub>0.2</sub>(Fe<sub>x</sub>Co<sub>1-x</sub>)<sub>0.8</sub>, Gd<sub>0.2</sub>(Co<sub>x</sub>Ni<sub>1-x</sub>)<sub>0.8</sub>, and Gd<sub>0.2</sub>(Fe<sub>x</sub>Ni<sub>1-x</sub>)<sub>0.8</sub>. *Phys. Rev. B* **22**, 1320–1326 (1980).
- Park, J. et al. Unconventional magnetoresistance induced by spin magnetism in GdFeCo. *Phys. Rev. B* **103**, 014421 (2021).
- Konar, B., Kim, J. & Jung, I.-H. Critical systematic evaluation and thermodynamic optimization of the Fe-RE system: RE = Gd, Tb, Dy, Ho, Er, Tm, Lu, and Y. *J. Phase Equilibria Diffus.* **38**, 509–542 (2017).
- Bernstein, G. & Guegnon, C. Aging phenomena in TbFe thin films. *J. Appl. Phys.* **55**, 1760–1762 (1984).
- Hansen, P. Chapter 4 magnetic amorphous alloys. *Handb. Magn. Mater.* **6**, 289–452 (1991).

**Publisher's note** Springer Nature remains neutral with regard to jurisdictional claims in published maps and institutional affiliations.

© The Author(s), under exclusive licence to Springer Nature Limited 2022



## Methods

**Sample growth and device fabrication.** The magnetic stacks were grown by magnetron sputtering on Si/SiN chips. The samples employed for transmission X-ray microscopy were deposited on SiN membranes (200 nm) transparent to the X-rays. The Ar pressure during the growth was 3 mtorr, and the base pressure was lower than  $10^{-7}$  torr. The deposited stacks were SiN/Ta(3)/Pt(5)/RE-TM/Ta(5)/Pt(1), where RE-TM stands for  $\text{Gd}_x\text{Fe}_y\text{Co}_{(1-x-y)}$  (15),  $\text{Tb}_x\text{Co}_{(1-x)}$  (4) or a multilayer  $[\text{Tb}(0.25)/\text{Co}(0.25)]_x$ . The RE and TM elements of the GdFeCo and TbCo alloys were co-sputtered from elemental targets. The composition was varied by independently adjusting the power of the sputter guns, and the deposition rates were calibrated by X-ray reflectivity. Blanket film samples and devices were grown at the same time. The device fabrication was performed by lift-off and subtraction techniques. The polymethyl methacrylate resist was spun and baked at 180 °C for 10 minutes, exposed by electron-beam lithography and developed in a solution of methyl isobutyl ketone and isopropyl alcohol. Then, thin films were deposited on the patterned resist and lifted off. The second step of electron-beam lithography and the electron evaporation of Ti(25) defined the hard mask covering the dot (1  $\mu\text{m}$  wide and 500 nm wide for GdFeCo and TbCo, respectively). In this second lithography step, the resist baking was skipped to avoid annealing the ferrimagnetic layers. Next, the Ti mask protected the device during the ion milling of the surrounding material, which was etched down to the Ta(3)/Pt(5) bilayer. The current line was contacted by Ti(5)/Au(50) pads fabricated by optical lithography and electron evaporation. Finally, 100 nm of Al were deposited on the back of the membranes to provide a heat sink during the measurements.

**STXM.** The X-ray measurements were performed at the PolLux beamline of the Swiss Light Source (Paul Scherrer Institut, Switzerland) and at the Maxymus beamline of the BESSY II electron storage ring (Helmholtz-Zentrum Berlin, Germany). A current-pump, X-ray-probe approach was employed to excite and detect the magnetization dynamics with both spatial and temporal resolutions. The elemental sensitivity was provided by XMCD. Since this effect depends on the projection of the magnetization on the direction of the light polarization, the samples were oriented normally to the X-rays to probe the perpendicular component of the magnetization. The energy of the circularly polarized X-rays with negative helicity was tuned to the  $L_3$  and  $M_5$  absorption edges of the TM and RE elements, respectively (Fe, 707 eV; Co, 778 eV; Gd, 1,190 eV; Tb, 1,243 eV). Monochromatic X-ray pulses with a 500 MHz repetition rate were focused onto the sample by a Fresnel zone plate and an order-selecting aperture. A typical image comprised about  $35 \times 35$  pixels and was acquired by raster scanning the X-ray beam over an area of  $1.2 \times 1.2 \mu\text{m}^2$ , which corresponds to a spatial resolution of 35 nm. The transmitted photons were collected by an avalanche photodiode whose output was routed to a field-programmable gate array. The temporal resolution was determined by the duration of the X-ray pulses, on the order of 70 ps. The XMCD time traces were obtained by averaging the dichroic signal over the entire dot surface and then normalized to the steady-state signal.

The electric pulses were generated by an arbitrary waveform generator (Keysight M8195A, PolLux) or by a pulse-pattern generator (Keysight 81134A, Maxymus). The internal clock of these instruments was synchronized to the repetition rate of the light flashes (500 MHz, PolLux) or to the revolution frequency of the electron ring (1 MHz, Maxymus). The excitation pattern comprised sequences of set–reset pulses with similar amplitude and length and opposite polarity. The period of a set–reset unit was approximately 50 ns or 100 ns. The corresponding separation between the positive and negative pulses was usually set to 25 ns and 50 ns, respectively. The excitation was fed to a digital oscilloscope for monitoring purposes via a 20 dB pick-off tee. At each pixel, photons were collected typically for 500 ms; therefore each time trace was obtained by averaging the dynamics over  $\sim 10^{10}$  pulse sequences.

The device under testing was wire bonded to a printed circuit board, and its status was continually checked by monitoring its d.c. resistance. A 50  $\Omega$  resistor was connected in parallel to ensure the impedance matching. The in-plane magnetic field was controlled by an electro-mechanical magnet.  $\text{O}_2$  (PolLux) or He (Maxymus) at a pressure of 5–10 mbar was injected in the chamber prior to the measurements to improve the cooling of the devices and, in the case of  $\text{O}_2$ , limit the carbon deposition over the scanned area.

**Micromagnetic simulations.** The micromagnetic simulations were performed with a custom-made, mumax<sup>3</sup>-based code<sup>51</sup> that takes into account the individual sublattices (S1, Fe; S2, Gd) forming the ferrimagnetic dot (thickness, 15 nm; diameter, 512 nm). It solves the coupled Landau–Lifschitz–Gilbert equations of the two sublattices, linked by the antiferromagnetic coupling. The code includes the SOT and the STT. The Landau–Lifschitz–Gilbert equation of the  $i$ th = 1, 2 sublattice reads as follows:

$$\frac{d\mathbf{m}_i}{dt} = -\gamma_i \mathbf{m}_i \times \mathbf{H}_i^{\text{eff}} + \alpha_i \mathbf{m}_i \times \frac{d\mathbf{m}_i}{dt} + \boldsymbol{\tau}_i^{\text{SOT}} + \boldsymbol{\tau}_i^{\text{STT}} \quad (1)$$

where  $\mathbf{m}_i(\mathbf{r}, t)$  is the normalized local magnetization that changes in time ( $t$ ) and space ( $\mathbf{r}$ ).  $\mathbf{H}_i^{\text{eff}}$  is the total effective magnetic field, which includes the external

magnetic field, the effective anisotropy, the Dzyaloshinskii–Moriya interaction and the intra-lattice and inter-lattice exchange interactions. The latter is modelled by the antiferromagnetic exchange field  $\mathbf{H}_{\text{AF},i}$  given by  $\mathbf{H}_{\text{AF},i} = -\frac{1}{\mu_0 M_{s,i}} \frac{\delta E_{\text{ex}}}{\delta \mathbf{m}_i}$ , where  $M_{s,i}$  is the saturation magnetization and  $\mu_0$  the permeability of free space. Here,  $E_{\text{ex}} = -C_{\text{ex}} \mathbf{m}_1 \cdot \mathbf{m}_2$  is the energy density of the antiferromagnetic coupling, whose strength is determined by the parameter  $C_{\text{ex}}$ . In the present study, the latter was varied to reproduce the different experimental observations (Supplementary Note 7). In addition,  $\alpha_i$  and  $\gamma_i = \mu_0 g_i \mu_B / \hbar$  are the Gilbert damping and the gyromagnetic ratio of each sublattice, respectively, with  $g_i$  the Landé factor;  $\mu_B$  and  $\hbar$  are the Bohr magneton and the reduced Planck constant, respectively; and  $\boldsymbol{\tau}_i^{\text{SOT}}$  and  $\boldsymbol{\tau}_i^{\text{STT}}$  are the SOT and STT contributions. The details of the micromagnetic code can be found in ref. 33 and in Supplementary Note 8.

**STEM and EDX.** STEM and EDX measurements were performed on an FEI Titan Themis equipped with a probe spherical aberration corrector (DCOR, CEOS) and ChemiSTEM technology operated at 300 kV. A probe convergence semiangle of 18 mrad was used in combination with a collection angular range for the high-angle annular dark field detector set to 66–200 mrad.

Thin lamellas of the samples were cut in cross-section by means of an FEI Helios Nanolab 600i focused ion beam instrument at accelerating voltages of 30 and 5 kV after deposition of C and Pt protective layers. Two samples with nominally identical  $\text{Gd}_{31}\text{Fe}_{66}\text{Co}_3$  composition were compared. The first sample (aged), grown simultaneously with the device whose measurements are presented in Fig. 2a,b, was 30 months old at the time of the STEM measurements. The second sample (fresh) was grown four weeks before the characterization with the same recipe as the first sample. We estimated by Rutherford backscattering spectroscopy that the Gd concentration was the same in the two samples within an uncertainty of less than 2%.

The composition of the samples was evaluated by EDX mapping, and the elemental maps of the C K, N K, O K, Si K, Fe K, Co K, Ta L, Pt L and Gd L signals were extracted from the spectrum image. The elemental profiles of Fe and Gd across the  $\text{Gd}_{31}\text{Fe}_{66}\text{Co}_3$  layer thickness were calculated by averaging over the horizontal direction in Fig. 5a,d. The correlation image was obtained by calculating at each pixel  $i$  the quantity  $\frac{f_i - F}{s_f} \frac{g_i - G}{s_g}$ , where  $f_i$  ( $g_i$ ) is the  $i$ th pixel intensity in the map of Fe (Gd),  $F$  ( $G$ ) is the corresponding average image intensity and  $s_f$  ( $s_g$ ) is the standard deviation<sup>52</sup>. The correlation coefficient was then calculated as  $\frac{1}{N-1} \sum_{i=1}^N \left( \frac{f_i - F}{s_f} \right) \left( \frac{g_i - G}{s_g} \right)$ , where  $N$  is the number of pixels. As an alternative to this method, the correlation coefficient was also determined by comparing the intensity of the Fe and Gd STEM–EDX images, averaged along the vertical direction, as described in detail in Supplementary Note 13. Both approaches yield a higher anticorrelation in the fresh sample relative to the aged sample.

Nanobeam electron diffraction measurements were performed on the same set of GdFeCo samples<sup>53</sup>. The diffraction patterns were acquired in STEM mode by using the so-called microprobe mode (with the minicondenser lens excited), enabling an electron probe size of 2 nm to be focused onto the GdFeCo layer. For each sample, 270 diffraction patterns were recorded at different equidistant positions distributed in a rectangle of  $7 \times 42 \text{ nm}^2$ .

## Data availability

The datasets presented in this study are available from the corresponding authors upon reasonable request and in the ETH Research Collection at <https://doi.org/10.3929/ethz-b-000482072>.

## References

- Vansteenkiste, A. et al. The design and verification of MuMax3. *AIP Adv.* **4**, 107133 (2014).
- Johnson, G. R. et al. Investigations of element spatial correlation in Mn-promoted Co-based Fischer-Tropsch synthesis catalysts. *J. Catal.* **328**, 111–122 (2015).
- Hirata, A. & Chen, M. Angstrom-beam electron diffraction of amorphous materials. *J. Non Cryst. Solids* **383**, 52–58 (2014).

## Acknowledgements

We thank M. Baumgartner and C. Murer for fruitful discussions and help with the STXM measurements, and F. Binda for the assistance with the measurements at the vibrating sample magnetometer. We thank R. Erni for collaborating in the analysis of the diffraction measurements. We thank C. Vockenhuber for performing Rutherford backscattering measurements on GdFeCo and TbCo. This research was supported by the Swiss National Science Foundation (grant nos 200020\_200465 and PZ00P2-179944) and the Swiss Government Excellence Scholarship (ESKAS no. 2018.0056). The PolLux end station was financed by the German Ministerium für Bildung und Forschung (BMBF) through contracts 05K16WED and 05K19WE2. The work by E.M. and V.R. was supported by the Ministerio de Economía y Competitividad of the Spanish Government (project no. MAT2017-87072-C4-1-P) and by the Consejería de Educación of the Junta de Castilla y León (project nos SA299P18 and SA0114P20). We acknowledge the Paul Scherrer Institut, Villigen, Switzerland for provision of synchrotron radiation beamtime at beamline X07DA-PolLux of the Swiss Light Source. We also thank the



Helmholtz-Zentrum Berlin for the allocation of synchrotron radiation beamtime at the UE-46 Maxymus beamline.

### Author contributions

P.G., G.S. and C.-H.L. planned the experiment. G.S., C.-H.L., V.K. and G.K. performed the STXM measurements with the support of S.F., M.W. and J.R.; G.S. characterized the magnetic properties of the full films and devices. E.M. and V.R. developed the micromagnetic code and performed the simulations. M.R. performed the STEM characterization and the nanobeam diffraction measurements. M.R. and G.S. analysed the STEM-EDX maps. G.S. and P.G. analysed the data and wrote the manuscript with input from E.M. All authors discussed the data and commented on the manuscript.

### Competing interests

The authors declare no competing interests.

### Additional information

**Supplementary information** The online version contains supplementary material available at <https://doi.org/10.1038/s41563-022-01248-8>.

**Correspondence and requests for materials** should be addressed to Giacomo Sala or Pietro Gambardella.

**Peer review information** *Nature Materials* thanks Olena Gommonay, Xuepeng Qiu and the other, anonymous, reviewer(s) for their contribution to the peer review of this work.

**Reprints and permissions information** is available at [www.nature.com/reprints](http://www.nature.com/reprints).